A 3D numerical study of sweep gas effects as an operational strategy governing transport and performance in solid oxide electrolysis cells

Yongguk Kim[a], Dongkeun Lee[b], Jinyoung Park[c], Youngsang Kim[d], Wonyoung Lee[e] and Yonggyun Bae[f]

[a] Korea Institute of Machinery & Materials, Daejeon, South Korea, kimyg@kimm.re.kr
[b] Korea Institute of Machinery & Materials, Daejeon, South Korea, keun5832@kimm.re.kr
[c] Korea Institute of Machinery & Materials, Daejeon, South Korea, zeragon@kimm.re.kr
[d] Korea Institute of Machinery & Materials, Daejeon, South Korea, yskim@kimm.re.kr
[e] Dept. of Mechanical Eng., Sungkyunkwan Univ., Suwon-si, South Korea, leewy@skku.edu
[f] Korea Institute of Machinery & Materials, Daejeon, South Korea, ygbae@kimm.re.kr, CA

Abstract:

Three-dimensional coupled electrochemical computational fluid dynamics (CFD) simulations were performed to investigate the effects of sweep-gas composition on the internal reaction environment and operating voltage of a solid oxide electrolysis cell (SOEC). Electrochemical kinetic parameters were calibrated using 1 × 1 cm^2 button-cell experiments and validated using 10 × 10 cm^2 single-cell stack experiments. Under N_2 and H_2O sweep conditions, the operating voltage was lower than that under the conventional air-sweep condition, and the H_2O case showed the lowest voltage level. In contrast, the differences in the charge-transfer current distribution and temperature distribution remained limited. The O_2 mole fraction at the air electrode–electrolyte interface was substantially reduced under the non-air sweep conditions, and its spatial distribution directly corresponded to the reversible-potential distribution. As a result, the reversible potential decreased significantly under the N_2 and H_2O sweep conditions. Although the concentration overpotential increased under these low-oxygen sweep conditions, this was interpreted as a Nernst-type concentration effect caused by large local oxygen-partial-pressure changes rather than simply by deteriorated mass transport. These results indicate that the lower operating voltage under non-air sweep conditions is governed primarily by the reduced reversible potential induced by the lower oxygen partial pressure at the air electrode.

Keywords:

Computational fluid dynamics; Electrochemistry; Solid oxide electrolysis cell; Sweep gas.

1. Introduction

With the increasing deployment of renewable energy, power-supply intermittency is becoming more pronounced, thereby heightening the importance of green-hydrogen production technologies that can simultaneously support large-scale energy storage and enhanced grid flexibility. Among water-electrolysis technologies for hydrogen production, solid oxide electrolysis cells (SOECs) are regarded as a promising option because high-temperature operation reduces the thermodynamic driving voltage required for steam splitting while enabling rapid electrode kinetics. As a result, SOECs offer both high energy-conversion efficiency and strong scalability. In addition, their ability to utilize external heat sources and their reduced dependence on precious-metal catalysts further position SOECs as a next-generation high-efficiency electrolysis system [1]. However, under practical operating conditions, average performance metrics alone are not sufficient to guarantee cell integrity or long-term stability, because non-uniform local reaction environments developed within the electrodes can act as a critical limiting factor. Solid oxide electrochemical systems operate through the coupled interaction of heat transfer, fluid flow, species transport, charge transport, and electrochemical reactions; accordingly, variations in temperature and gas-species distributions directly influence reaction distributions and overpotential formation. This issue is particularly important at the oxygen electrode, where oxygen generated at the electrode–electrolyte interface must pass through the porous electrode and be discharged into the gas channel. When oxygen accumulation and concentration gradients

develop during this process, both the local reaction driving force and the mass-transport resistance can change simultaneously. Therefore, oxygen-electrode losses are not determined solely by the intrinsic properties of the electrode materials, but are also strongly governed by how the oxygen partial pressure and gas composition imposed at the channel side interact with transport processes inside the electrode. In this context, Barelli et al. applied steam as an oxygen-electrode sweep gas and demonstrated its feasibility at the single-cell level, together with the possibility of condensation-based oxygen recovery [2]. Im-orb et al. showed, through flowsheet-based analysis under oxygen, air, and steam conditions, that the type of sweep gas can affect the equilibrium potential, overpotentials, energy demand, and overall efficiency [3]. Sun et al. introduced steam sweep gas as an operational strategy in an rSOC(reversible Solid Oxide Cell) system analysis and highlighted its potential for reducing overpotential losses while enabling oxygen recovery [4]. Chen and Jeng proposed a system concept in which nitrogen oxide was employed as a sweep gas to couple hydrogen production with greenhouse-gas treatment [5]. Meanwhile, Wierzbicki et al. reported, from long-term tests under O_2, N_2, and steam conditions, that sweep-gas composition can also influence degradation behavior [6]. Nevertheless, these studies were focused primarily on the feasibility of sweep-gas application, system efficiency and thermal balance, process integration, or long-term degradation comparisons. It is therefore necessary to examine, at the electrode-resolved level, how changes in sweep-gas composition modify the oxygen partial pressure and oxygen distribution inside the porous oxygen electrode through channel-side boundary conditions, and how these changes subsequently restructure the mass-transport overpotential, current-density distribution, temperature distribution, and thermal gradients. In the present study, three-dimensional coupled electrochemical computational fluid dynamics(CFD) simulations were performed for air- and H_2O-sweep conditions to spatially analyze oxygen partial pressure and oxygen distribution within the porous oxygen electrode and to correlate them with the distributions of mass-transport overpotential, current density, temperature, and thermal gradients. Figure 1(a) presents a schematic comparison between conventional air-sweep SOEC operation and steam-sweep SOEC operation. Under the conventional air-sweep condition, the generated oxygen is discharged together with nitrogen, whereas under the steam-sweep condition, the exhaust consists of a mixture of oxygen and steam. This difference in channel-side composition can, in turn, lead to distinct transport and reaction environments within the oxygen electrode. On this basis, the present work aims to clarify, from a physical standpoint, how sweep-gas composition governs internal transport behavior and electrochemical performance at the oxygen electrode.

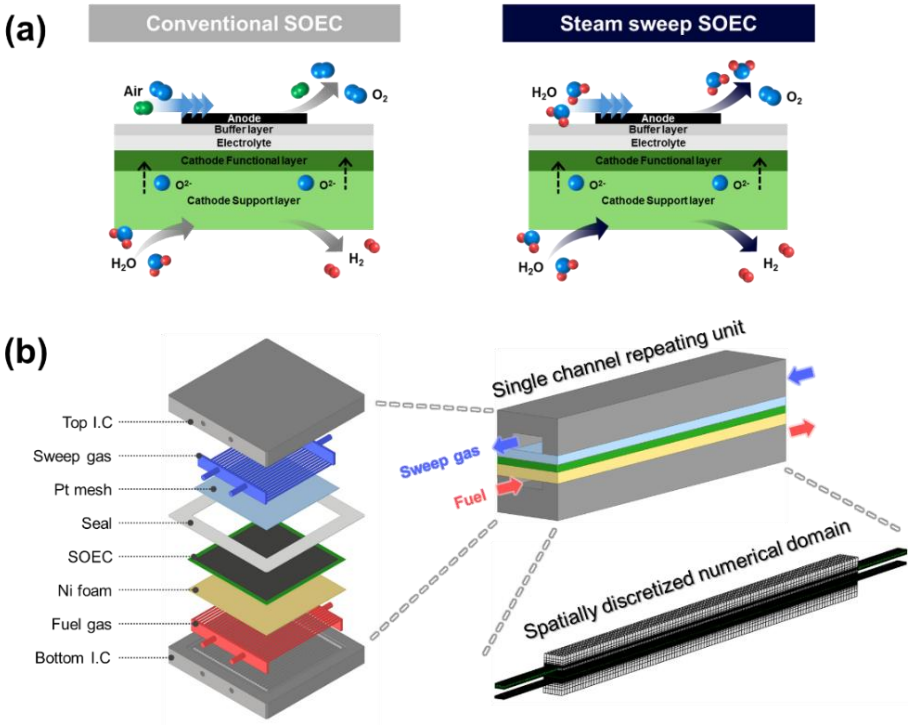

Figure 1. Schematic illustrations of the sweep-gas operating concepts, computational domain, and mesh used in this study: (a) comparison of a conventional air-sweep SOEC and a steam-sweep SOEC; (b) exploded view of the repeating unit and schematic of the single-channel computational domain; and

representative mesh configuration. The geometry in (b) is shown for illustrative purposes only and does not represent the actual scale.

2. Model description

To analyze the reaction and transport phenomena occurring within the SOEC electrodes under different sweep-gas compositions, a three-dimensional multiphysics coupled CFD model was developed in this study. The model was constructed to resolve, in an integrated manner, heat transfer, fluid flow, species transport, charge transport, and electrochemical reactions occurring simultaneously within the SOEC repeating unit. In particular, thermal, fluid, chemical, and electrochemical phenomena were all modeled in a fully resolved three-dimensional framework. On this basis, the effects of sweep-gas conditions on the reaction environment and transport behavior within the oxygen electrode were quantitatively examined in space. The details of the present model are described in the following order: geometry of the computational domain, governing equations, boundary and operating conditions, and numerical procedure.

2.1. Geometry and computational domain

Figure 1(b) shows the repeating unit of the commercial-level planar cathode-supported SOEC stack used in the present analysis. To ensure both computational reliability and efficiency, a channel-level repeating unit was selected as the computational domain. Because this channel-level repeating unit is symmetrically repeated in the channelwise and spanwise directions to form the full SOEC stack repeating unit, it can be regarded as the minimum computational domain that mathematically represents the entire repeating unit. Accordingly, the present domain provides an appropriate representation of the local reaction environment and internal transport phenomena in a commercial planar SOEC stack. The repeating unit considered in this study consisted of a cathode-supported SOEC single cell, Ni foam as the current collector on the fuel-electrode side, Pt mesh as the current collector on the oxygen-electrode side, and metallic interconnectors with channel-and-rib structures. The fuel and sweep gas were arranged in a counter-flow configuration. This flow arrangement reflects practical stack operating conditions and, at the same time, enables clearer analysis of the spatial non-uniformities in temperature and species distributions developed along the fuel and oxygen electrodes. The commercial cathode-supported planar SOEC used in this study was the Elcogen 400B cell manufactured by Elcogen. The total cell area was 12 × 12 cm², and the active area was 10 × 10 cm². The Elcogen 400B consists of a fuel-electrode support layer and functional layer (FESL and FEFL) made of Ni– Yttria-stabilized zirconia (YSZ) cermet, a YSZ electrolyte, a Gadolinium-doped ceria (GDC) interlayer, and an LSC-based oxygen-electrode functional layer and current-collecting layer (OEFL and OECL), where LSC serves as a mixed ionic-electronic conductor [7].

2.2. Governing equations and model assumptions

To describe the electrochemical reactions and thermo-fluid coupled phenomena occurring within the SOEC repeating unit, a three-dimensional multiphysics coupled analysis was performed by simultaneously solving the conservation equations for mass, momentum, species, energy, and charge. The electrode reaction rate was calculated using a modified Butler–Volmer equation, and the resulting reaction rate was incorporated into the corresponding conservation equations as species, heat, and charge source terms. In this way, channel flow, species transport within the porous electrodes, current distribution, overpotential formation, and temperature distribution were analyzed in a fully coupled manner. The detailed governing equations are listed in Table 1 [8]. The gas flow field was solved in both the channel and porous-electrode regions. Laminar flow was assumed in the channels, whereas the porous-electrode regions were treated by accounting for flow resistance arising from the pore structure together with effective transport properties. Species transport was described by considering both convection and diffusion, while charge transport was calculated separately in the electronically conducting and ionically conducting phases. The energy equation was used to account for heat transfer in both the gas and solid regions, together with heat generation associated with electrochemical reactions. In particular, to examine the influence of sweep-gas composition on oxygen distribution and mass-transport overpotential within the oxygen electrode, the model was formulated such that local variations in temperature and gas composition directly affected the reaction rate and potential distribution. To ensure computational efficiency and numerical convergence, the following assumptions were applied.

1. All repeating units were assumed to operate under steady-state conditions.

2. The porous electrodes were treated as macroscopically homogeneous porous media, and the solid and gas phases were assumed to be in local thermal equilibrium.
3. All gases were assumed to behave as ideal gases, and the major thermophysical properties were represented as temperature-dependent functions.
4. The outlet pressure of the channel was set to atmospheric pressure, and the inlet and outlet channels were sufficiently extended to minimize the influence of flow development and to prevent numerical instability caused by back-flow.
5. Thermal radiation within the repeating unit was neglected.

Table 1. Governing equations for repeating-unit simulations.

Governing equation		**Source term**	
Mass conservation	$\nabla \cdot (\rho\vec{u}) = \dot{S}_m$	$\dot{S}_m = \frac{(M_{H_2O} - M_{H_2})R_a}{2F}$	(at Fuel electrode)
		$\dot{S}_m = -\frac{M_{O_2}R_c}{4F}$	(at Air electrode)
		$\dot{S}_m = 0$	(at CH, IC, CC)
Momentum conservation	$\nabla \cdot \left(\frac{\rho\vec{u}\vec{u}}{\varepsilon}\right) = -\varepsilon\nabla p + \nabla \cdot \left[\mu(\nabla\vec{u} + \nabla\vec{u}^T) - \frac{2}{3}\mu\nabla\vec{u}\right] + \varepsilon\vec{F}_{Da}$	$\vec{F}_{Da} = -\frac{\mu}{\zeta}\vec{u}$	(at all electrode, CC)
		$\vec{F}_{Da} = 0$	(at CH, IC)
Species conservation	$\nabla \cdot (\rho\omega_i\vec{u}) = \nabla \cdot \left(\rho D_i^{eff}\nabla\omega_i\right) + \dot{S}_i$	$\dot{S}_{H_2} = -\frac{M_{H_2}R_a}{2F}$ $\dot{S}_{H_2O} = \frac{M_{H_2O}R_a}{2F}$	(at Fuel electrode)
		$\dot{S}_{O_2} = -\frac{M_{O_2}R_c}{4F}$	(at Air electrode)
		$\dot{S}_i = 0$	(at CH, IC, CC)
Energy conservation	$\nabla \cdot \left(\rho\vec{u}h_{sen}^{eff}\right) = \nabla \cdot \left(k^{eff}\nabla T - \sum_i h_{sen,i}\vec{J}_i\right) + \dot{S}_h$	$\dot{S}_h = 0$	(at CH)
		$\dot{S}_h = \sigma_{ele}^{eff}\left(\vec{\nabla}\phi_{ele}\right)^2$	(at IC, CC)
		$\dot{S}_h = \sigma_{ion}^{eff}\left(\vec{\nabla}\phi_{ion}\right)^2$	(at EL)
		$\dot{S}_h = \sigma_{ion}^{eff}\left(\vec{\nabla}\phi_{ion}\right)^2 + \sigma_{ele}^{eff}\left(\vec{\nabla}\phi_{ele}\right)^2$	(at IL)
		$\dot{S}_h = \sigma_{ele}^{eff}\left(\vec{\nabla}\phi_{ele}\right)^2 + \sigma_{ion}^{eff}\left(\vec{\nabla}\phi_{ion}\right)^2 + Si\left(\lvert\eta_{act}\rvert - T\frac{\delta\phi_{rev}}{\delta T}\right)$	(at all electrode)
Charge Conservation	$\nabla \cdot i_{elec} = \nabla \cdot \left(-\sigma_{elec}^{eff}\nabla\phi_{\mathrm{elec}}\right) = \dot{Q}_{elec}$	$\dot{Q}_{elec} = -R_a$	(at Fuel electrode)
		$\dot{Q}_{elec} = -R_c$	(at Air electrode)
		$\dot{Q}_{elec} = 0$	(at CH, IC, CC)
	$\nabla \cdot i_{ion} = \nabla \cdot \left(-\sigma_{ion}^{eff}\nabla\phi_{ion}\right) = \dot{Q}_{ion}$	$\dot{Q}_{elec} = R_a$	(at Fuel electrode)
		$\dot{Q}_{elec} = R_c$	(at Air electrode)
		$\dot{Q}_{elec} = 0$	(at CH, IC, CC)

2.3. Boundary conditions and operating conditions

At the gas-channel inlet, a mass-flow inlet boundary condition was imposed to specify the flow rate, temperature, and gas-mixture composition, and the composition of each species was prescribed on a molar-fraction basis. The channel outlet was set to atmospheric pressure, and all external walls of the repeating unit were treated as adiabatic boundaries. These conditions were adopted to provide a consistent basis for comparing the internal reaction and transport phenomena within the repeating unit. For the electrical boundary conditions, the bottom of the cathode-side current collector (IC) was assigned as the ground, whereas a fixed-current condition was imposed at the top of the anode-side IC. In addition, the charge-transfer current was constrained to remain continuous across the two electrodes so that overall charge conservation was satisfied. Zero ionic-potential flux was imposed at the bottom of the cathode IC and at the top of the anode IC. With this configuration, the charge-transport paths through the external current collectors and the electrolyte could be distinguished, while the potential and current distributions were calculated under galvanostatic operation. The target operating temperature was set to 700 °C. On the fuel-electrode side, a 50% humidified fuel composed of 50 mol% H_2 and 50 mol% H_2O was supplied at 3.346 LPM. On the oxygen-electrode side, air, N_2, and H_2O were considered as sweep gases, and the total flow rate was fixed at 0.836 LPM. To compare the effect of sweep-gas composition, three conditions were considered for each case: 100% air, 0.01% O_2 mixed with 99.99% N_2 or H_2O. The system pressure was fixed at 1 atm, and the operating current density was analyzed 0.5 A cm^{-2}. The detailed operating conditions are listed in Table 2.

Table 2. Operating conditions for repeating-unit simulations.

Operating conditions		**Value**
External current density load		0.5 A/cm^2
Temperature		973.15 K
Pressure		1 atm
Inlet flow rate	Fuel	3.346 lpm (Constant flow rate)
	Sweep	0.836 lpm (Constant flow rate)
Inlet fuel composition	Fuel	H_2 : H_2O = 50 % : 50 %
	Sweep	Air (O_2 21 % : N_2 79 %)
		N_2 100 %
		H_2O 100 %

2.4. Numerical procedure

The SOEC repeating-unit analysis was performed using the commercial CFD code ANSYS Fluent. In Fluent, the continuity, momentum, species-conservation, and energy equations were solved to obtain the temperature, pressure, and gas-composition fields. The calculated local physical quantities were then passed to in-house developed user-defined functions (UDFs), where the electrochemical reactions were evaluated based on the electron/ion charge-conservation equations and the modified Butler–Volmer equation. The resulting current and reaction source terms were subsequently fed back into the governing equations in Fluent and recalculated. Through this iterative procedure, the final converged solution was obtained. Accordingly, the present analysis was carried out in a three-dimensional multiphysics coupled framework in which fluid flow, heat transfer, species transport, and electrochemical reactions were mutually coupled through feedback. For pressure–velocity coupling, the Semi-implicit method for pressure linked equations (SIMPLE) algorithm was employed. In the spatial discretization, the Green–Gauss cell-based scheme was used for gradient evaluation, and second-order upwind schemes were applied to pressure, density, momentum, species, energy, electrical potential, and ionic potential. To ensure stable convergence, the default under-relaxation factors were used for pressure, density, body force, energy, electrical potential, and ionic potential, whereas that for species was adjusted to 0.9995. The computational mesh consisted of approximately 1.1×10^6 elements. To achieve both computational efficiency and spatial resolution, different mesh sizes were assigned to the electrode and channel regions. In particular, a refined mesh was employed in the thickness direction near the electrode–electrolyte interfaces so that the reaction and potential gradients could be sufficiently resolved. A grid bias was also introduced in the thickness direction, and the size of the first cell was matched across neighboring regions to ensure both physical continuity and numerical stability at the interfaces. In addition, a non-uniform mesh was used by distinguishing regions that required high resolution from those with relatively mild variations,

thereby reducing the computational cost while preserving the key physical features. Node alignment was implemented at the interfaces so that stable calculations could be achieved even under non-conformal mesh conditions. The calculations were performed until all residuals fell below 1×10^{-7}, while the residual for the energy equation was reduced below 1×10^{-12}. To improve computational efficiency, 6-core parallel computation was employed, and the domain was partitioned along the main flow direction. A Gauss–Seidel smoother was used for the algebraic multigrid solver.

3. Results and discussion

3.1. Calibration of electrochemical kinetic parameters and model validation using 1 × 1 cm² button-cell and 10 × 10 cm² single-cell stack experiments

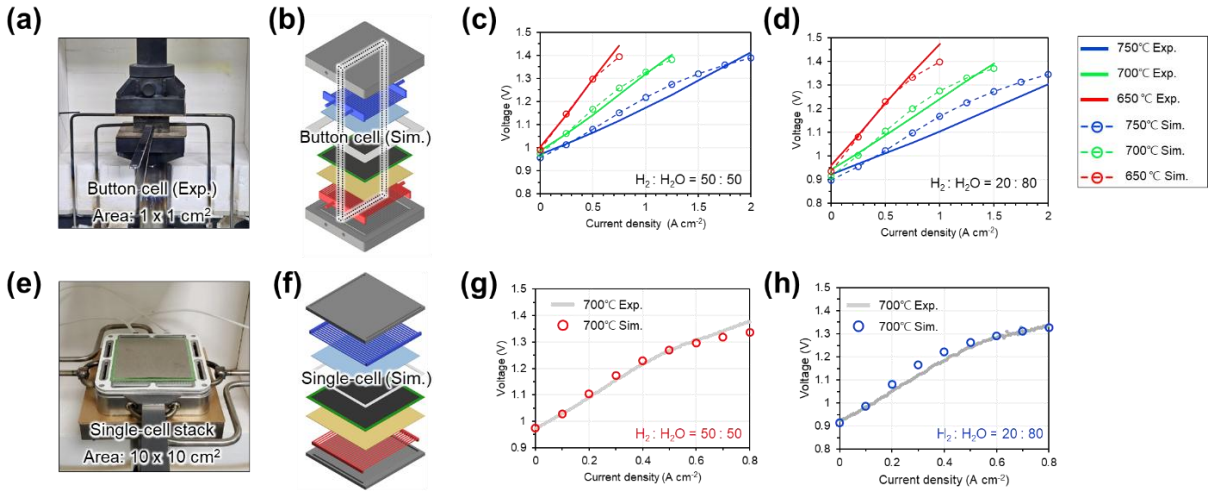

Figure 2. Calibration of electrochemical kinetic parameters and model validation using 1 × 1 cm² button-cell experiments and 10 × 10 cm² single-cell stack experiments. (a) Photograph of the button-cell experimental setup. (b) Schematic of the corresponding button-cell simulation geometry. Experimental and simulated I–V curves of the button cell under (c) 50 % H_2 + 50 % H_2O and (d) 20 % H_2 + 80 % H_2O at 650, 700, and 750 °C. (e) Photograph of the 10 × 10 cm² single-cell stack experimental setup. (f) Schematic of the corresponding single-cell simulation geometry. Experimental and simulated I–V curves of the 10 × 10 cm² single-cell stack at 700 °C under (g) 50 % H_2 + 50 % H_2O and (h) 20 % H_2 + 80 % H_2O.

Figure 2 presents the calibration of electrochemical kinetic parameters and the validation of the numerical model using 1 × 1 cm² button-cell and 10 × 10 cm² single-cell stack experiments. Figure 2(a) shows a photograph of the button-cell experimental setup, and Figure 2(b) presents the corresponding button-cell simulation geometry. Figures 2(c) and (d) compare the experimental and simulated results of the button cell under H_2 50% + H_2O 50% and H_2 20% + H_2O 80% conditions, respectively, over the temperature range of 650–750 °C. In addition, Figure 2(e) shows a photograph of the 10 × 10 cm² single-cell stack experimental setup, and Figure 2(f) presents the corresponding single-cell simulation geometry. Figures 2(g) and (h) compare the experimental and simulated results of the single-cell stack at 700 °C under H_2 50% + H_2O 50% and H_2 20% + H_2O 80% conditions, respectively. The electrochemical kinetic parameters were first calibrated using the button-cell experimental results and were then directly applied to the single-cell stack simulations without further adjustment. As a result, good agreement was obtained between the experimental and simulated results even under the single-cell stack conditions. These results indicate that the calibrated kinetic parameters are not limited to the button-cell level but remain valid under large-area single-cell conditions, thereby supporting the reliability of the subsequent repeating-unit simulation results.

3.2. Operating voltage distribution

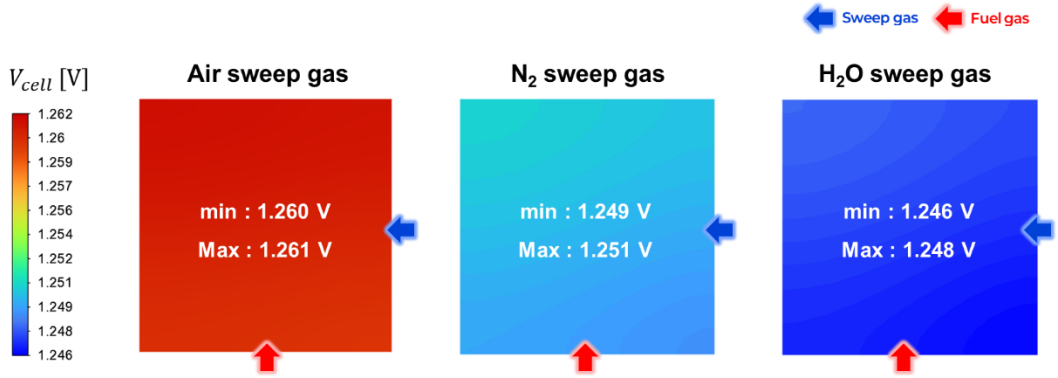

Figure 3. Operating voltage distribution at top interconnector tap under different sweep gas conditions

Figure 3 shows the local operating-voltage distribution under air, N_2, and H_2O sweep-gas conditions. In all three cases, the spatial voltage deviation remains limited, whereas the absolute voltage level differs clearly. Compared with the air case, the N_2 and H_2O sweep conditions exhibit lower operating voltages over the entire top interconnector tap, and the H_2O case shows a slightly lower voltage than the N_2 case. This trend is consistent with the I–V behavior presented above and spatially confirms that the non-air sweep conditions enable the same hydrogen production rate to be achieved at a lower voltage. The following sections investigate whether this operating-voltage difference arises from changes in the charge-transfer current or temperature field, or is governed mainly by the O_2 mole fraction and reversible-potential distributions at the air-electrode interface.

3.3. Charge-transfer current distribution

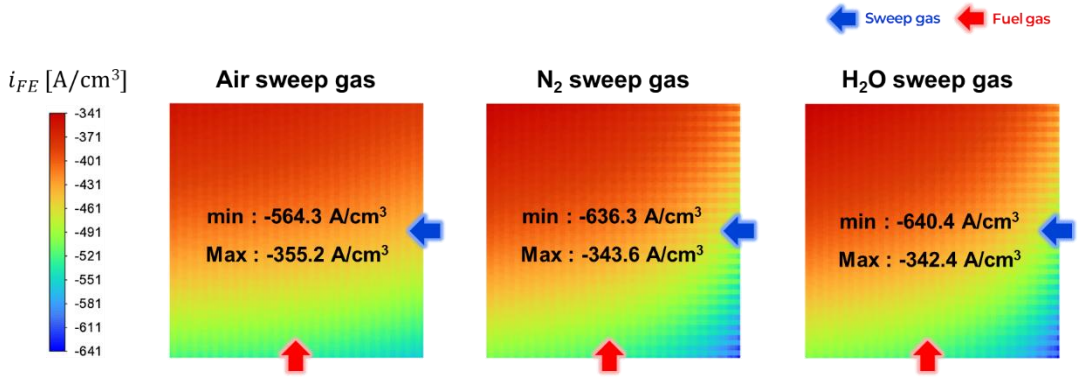

Figure 4. Charge-transfer current distribution at the fuel electrode under different sweep gas conditions.

Figure 4 shows the charge-transfer current distribution at the fuel electrode under air, N_2, and H_2O sweep-gas conditions. In all three cases, the charge-transfer current exhibits a common trend of increasing away from the fuel inlet. Under the N_2 and H_2O sweep-gas conditions, the influence of the sweep-gas flow direction is additionally reflected, resulting in a slightly stronger current concentration in the region farthest from both the fuel inlet and the sweep-gas inlet compared with the air case. However, the changes in the maximum-to-minimum difference and in the overall spatial distribution pattern remain limited, and the difference between the N_2 and H_2O cases is also small. In other words, although the type of sweep gas causes some redistribution of the charge-transfer current, the magnitude of this difference is not large enough to directly account for the overall performance difference.

3.4. Temperature distribution

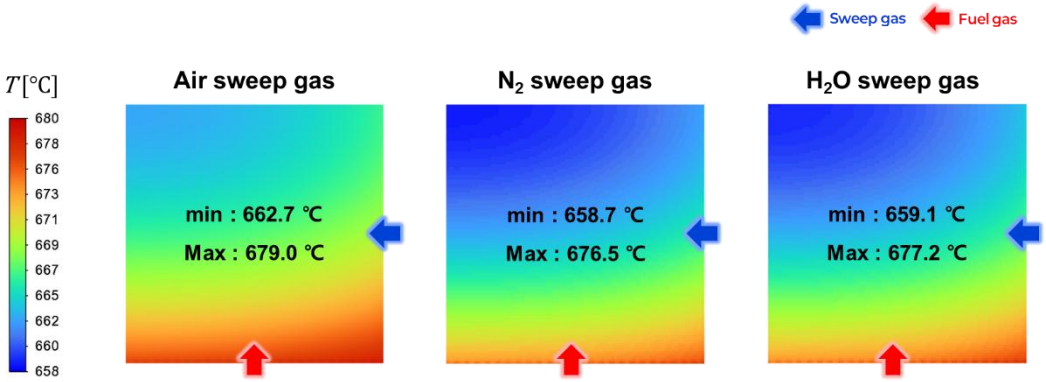

Figure 5. Temperature distribution at the fuel electrode – electrolyte interface under different sweep gas conditions.

Figure 5 shows the temperature distribution at the fuel electrode–electrolyte interface under air, N_2, and H_2O sweep-gas conditions. The air case exhibits the highest overall temperature level, whereas the N_2 and H_2O cases show very similar distributions. The maximum–minimum temperature difference also remains comparable in all three cases, at approximately 16–18 °C, indicating that the variation in thermal non-uniformity with sweep-gas composition is limited. Therefore, although the temperature field is slightly affected by the sweep-gas type, this effect is unlikely to be the primary cause of the performance difference observed in the present study.

3.5. Species (O_2) distribution

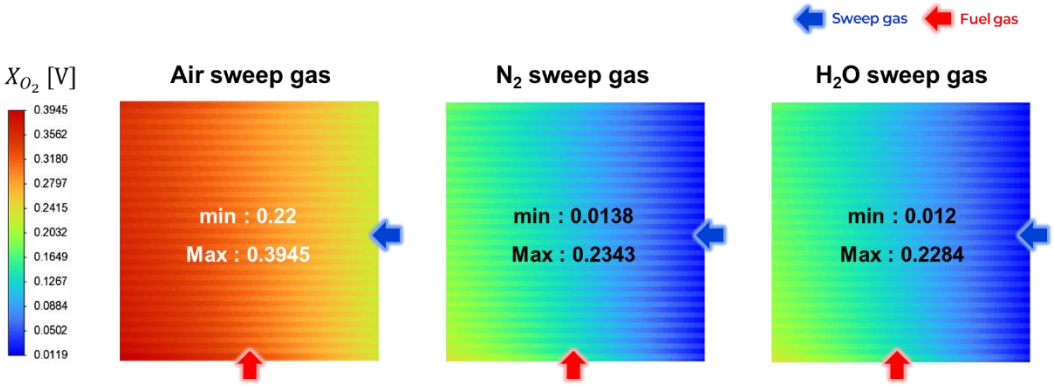

Figure 6. Species(O_2) distribution at the air electrode – electrolyte interface under different sweep gas conditions.

Figure 6 shows the O_2 mole-fraction distribution at the air electrode–electrolyte interface under air, N_2, and H_2O sweep-gas conditions. In all three cases, the O_2 mole fraction exhibits a common trend of increasing from the sweep-gas inlet toward the outlet because oxygen generated by the electrochemical reaction gradually accumulates along the sweep-gas flow direction. However, a significant difference appears in the absolute O_2 mole-fraction level between the air case and the N_2/H_2O cases. Under the air-sweep condition, the inlet gas already contains approximately 21% oxygen, so the interfacial O_2 mole fraction starts from a relatively high value and remains high throughout the domain. In contrast, under the N_2 and H_2O sweep conditions, no oxygen is present in the inlet gas, and therefore the interfacial O_2 mole fraction starts from a very low level and then gradually increases only as oxygen is generated and accumulated by the electrochemical reaction. In fact, the minimum interfacial O_2 mole fraction is about 0.22 in the air case, whereas it decreases to approximately 0.0138 and 0.012 in the N_2 and H_2O cases, respectively. Meanwhile, the difference between the N_2 and H_2O cases is relatively small, and both exhibit strongly diluted oxygen distributions compared with the air case. These results indicate that the sweep-gas composition directly restructures the local oxygen partial pressure

at the air-electrode interface, which provides the most direct basis for explaining the difference in the reversible-potential distribution discussed in the following section.

3.6. Reversible-potential distribution

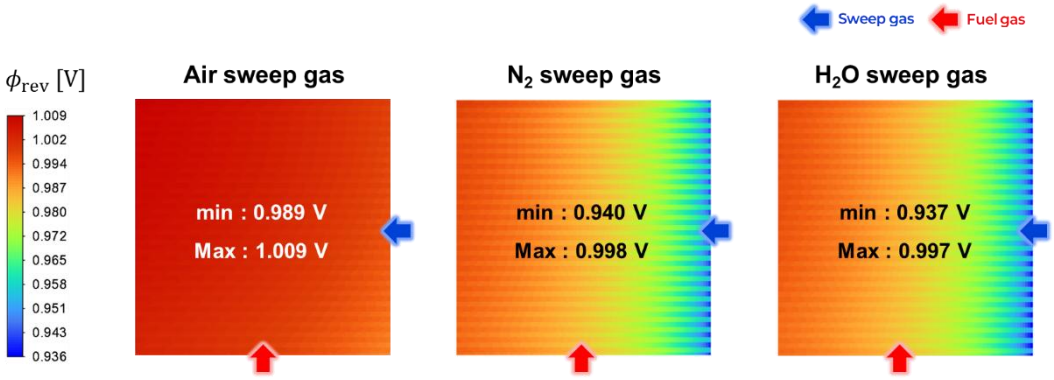

Figure 7. Reversible potential distribution at the air electrode under different sweep gas conditions.

Figure 7 shows the reversible-potential distribution at the air electrode under air, N_2, and H_2O sweep-gas conditions. The reversible potential is determined by temperature and the partial pressures of H_2, H_2O, and O_2. In the present comparison, the fuel-side H_2/H_2O conditions are identical in all cases, and therefore the main varying factors are the local temperature and the O_2 partial pressure at the air electrode. As shown in Figure 5, the N_2 and H_2O sweep cases exhibit slightly lower temperatures than the air case. If the temperature effect were dominant, this decrease would tend to increase the reversible potential. Nevertheless, Figure 7 clearly shows that the reversible potential is substantially lower under the N_2 and H_2O sweep conditions than under the air condition. This indicates that, under the present conditions, the reduction in O_2 mole fraction at the air electrode has a much stronger influence on the reversible potential than the temperature change. This interpretation is directly supported by the O_2 mole-fraction distribution shown in Figure 6. Under the air-sweep condition, the inlet gas already contains oxygen, and therefore a relatively high O_2 mole fraction and O_2 partial pressure are maintained at the air-electrode interface. In contrast, under the N_2 and H_2O sweep conditions, no oxygen is present in the inlet gas, so the interfacial O_2 mole fraction starts from a very low level and then gradually increases as oxygen generated by the electrochemical reaction accumulates along the sweep-gas flow direction. In fact, the spatial trend of the reversible-potential distribution in Figure 7 closely follows that of the O_2 mole-fraction distribution in Figure 6, demonstrating that the difference in interfacial O_2 mole fraction directly governs the formation of the reversible potential. In addition, the small difference in reversible potential between the N_2 and H_2O cases is also consistent with the limited difference in their O_2 mole-fraction distributions. Consequently, the lower operating voltage observed under the N_2 and H_2O sweep conditions, compared with the air case, can be interpreted primarily as a result of the reduced reversible potential caused by the lower O_2 partial pressure at the air electrode. In other words, the change in sweep-gas composition modifies the cell-voltage characteristics mainly by restructuring the O_2 mole fraction and reversible potential at the air-electrode interface, rather than by inducing large changes in the charge-transfer current distribution or the temperature field.

3.7. Overpotential distribution

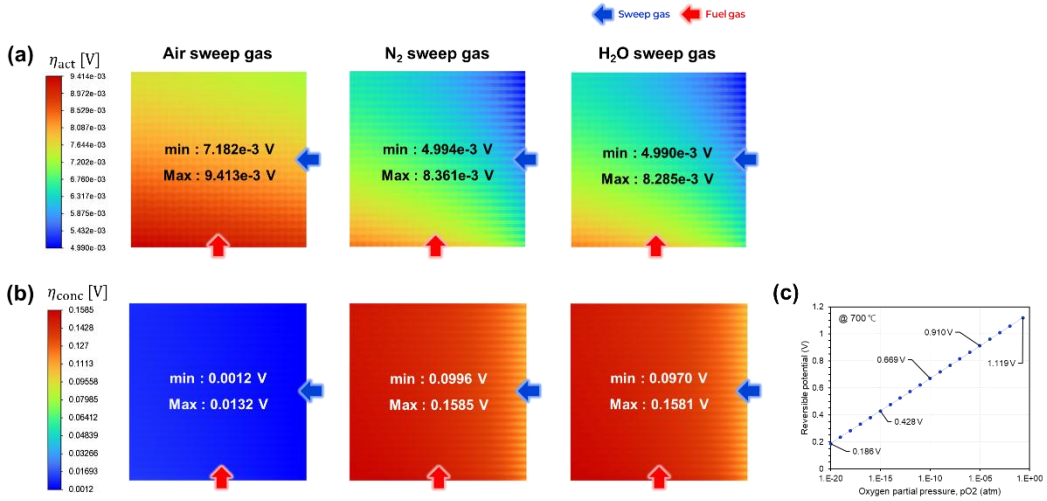

Figure 8. Overpotential distributions at the air electrode–electrolyte interface under different sweep gas conditions and the theoretical reversible potential at 700 °C: (a) activation overpotential, (b) concentration overpotential, and (c) reversible potential as a function of oxygen partial pressure.

Figure 8 shows the overpotential distributions at the air electrode–electrolyte interface under air, N_2, and H_2O sweep-gas conditions, together with the theoretical reversible potential at 700 °C. As shown in Figure 8(a), the activation overpotential exhibits some variation with sweep-gas type, but the difference in both its absolute magnitude and spatial deviation remains very small. In contrast, the concentration overpotential in Figure 8(b) shows a pronounced difference between the air case and the N_2/H_2O cases. This should not be interpreted simply as a deterioration of mass transport under the non-air sweep conditions. Rather, because the N_2 and H_2O cases start from very low initial oxygen partial pressures, the oxygen generated during operation causes a relatively large local increase in oxygen partial pressure. As shown in Figure 8(c), in the low-oxygen-partial-pressure region at 700 °C, even a small increase in oxygen partial pressure leads to a rapid recovery of the reversible potential. Therefore, although the absolute oxygen partial pressure remains lower than that in the air case, the larger difference between the reference state and the local state causes a substantial increase in the concentration overpotential under the N_2 and H_2O sweep conditions. Nevertheless, from the viewpoint of the overall cell voltage, the reduction in reversible potential induced by the lower oxygen partial pressure is more dominant than the increase in concentration overpotential. In other words, the lower operating voltage observed under the non-air sweep conditions is governed primarily by the reduced reversible potential rather than by the difference in activation overpotential, while the increase in concentration overpotential is more appropriately understood as a Nernst-type concentration effect caused by the local oxygen-partial-pressure change under low-oxygen sweep conditions

4. Conclusion

In this study, electrochemical kinetic parameters were calibrated and validated using 1 × 1 cm^2 button-cell experiments and 10 x 10 cm^2 single-cell stack experiments, and the internal reaction environment and performance of an SOEC under Air, N_2, and H_2O sweep-gas conditions were analyzed by three-dimensional coupled electrochemical CFD simulations. The N_2 and H_2O sweep conditions yielded lower operating voltages than the air case, and the H_2O case showed the lowest voltage level. In contrast, the differences in the charge-transfer current distribution and temperature distribution remained limited, indicating that these variables are not large enough to directly explain the performance difference observed in the present study. The O_2 mole-fraction distribution at the air electrode–electrolyte interface showed a large difference between the air case and the N_2/H_2O cases, and this distribution trend was closely consistent with the reversible-potential distribution. In other words, the reversible potential was substantially reduced in the N_2 and H_2O sweep conditions because of the lower oxygen partial pressure at the air-electrode interface, and this became the most direct cause of the reduced operating voltage. In addition, the difference in activation overpotential was small, whereas the concentration overpotential became much larger under the non-air sweep conditions. However, this should be interpreted not as a simple increase in mass-transport resistance, but as the result of a large local oxygen-partial-pressure change under very low initial oxygen-partial-pressure conditions, which is reflected in the Nernst concentration term. Therefore, sweep-gas composition should be regarded not merely as a product-removal condition, but as a key operating parameter that governs the operating voltage and internal reaction environment of the SOEC by restructuring the O_2 partial pressure and reversible potential at the air-electrode interface.

Nomenclature

A	Pre-exponential factor, A·m^{-2}
C_p	Heat capacity, J/(kg K)
D_i	Effective diffusivity of species i, m^2/s
D_{ij}	Binary diffusivity between species i and j, m^2/s
$D_{kn,i}$	Knudsen diffusivity of species i, m^2/s
$D_{mix,i}$	Mixture-averaged diffusivity of species i, m^2/s
E	Activation energy, J/mol
F	Faraday constant, C/mol
F_{Da}	Darcy friction force, N/m^3
h_{sen}	Specific sensible enthalpy, J/kg
i	Current density, A/cm^2
i_0	Exchange current density, A/cm^2
J_i	Diffusion flux of species i, kg/(m^2 s)
k	Thermal conductivity, W/(m K)
M_i	Molecular weight of species i, kg/mol
p	Pressure, N/m^2
$\dot{Q}$	Volumetric charge current source, A/cm^3
$\dot{q}$	Heat transfer rate, W
R	Ideal gas constant, J/(mol K)
$\dot{S}_h$	Volumetric heat source, W/m^3
$\dot{S}_i$	Volumetric species source, kg/(m^3 s)
$\dot{S}_m$	Volumetric mass source, kg/(m^3 s)
T	Temperature, K
u	Velocity, m/s
x_i	Molar fraction of species i, −

Greek symbols

ε	Porosity, −
ζ	Permeability, m^2
η	Overpotential, V
μ_i	Dynamic viscosity of species i, kg/(m s)
ρ	Density, kg/m3
σ	Charged-species conductivity, S/m
τ	Tortuosity, −
ϕ	Electric potential, V
ω_i	Mass fraction of species i, −

Subscripts and superscripts

AE	Air electrode
eff	Effective
FE	Fuel electrode
i	Species i
$elec$	Electronic
ion	Ionic
Kn	Knudsen
mix	Mixture
rev	Reversible
0	Standard

Abbreviation

$OECL$	Oxygen electrode current collecting layer
$OEFL$	Oxygen electrode functional layer
CH	Channel
EL	Electrolyte
$FEEL$	Fuel electrode functional layer
$FESL$	Fuel electrode support layer
GDC	Gadolinium-doped ceria
IC	Interconnect
IL	Interlayer
LSC	Lanthanum strontium cobaltite
$SIMPLE$	Semi-implicit method for pressure linked equations
$SOEC$	Solid oxide electrolysis cell
UDF	User-defined function
YSZ	Yttria-stabilized zirconia

References

[1] Bang S., Yoo H.S., Kim J.G., Jung J.H., Kim D., Park J., Lee W., Sequential Core-Shell to Alloy Evolution Enables the Structural Stabilization and Catalytic Activation of Solid Oxide Electrolysis Cells. Advanced Functional Materials 2026;36(26):e202525596.

[2] Barelli L., Bidini G., Cinti G., Steam as sweep gas in SOE oxygen electrode. Journal of Energy Storage 2018;20:190-95.

[3] Im-orb K., Visitdumrongkul N., Saebea D., Patcharavorachot Y., Arpornwichanop A., Flowsheet-based model and exergy analysis of solid oxide electrolysis cells for clean hydrogen production. Journal of Cleaner Production 2018;170:1-13.

[4] Sun Y., Qian T., Zhu J., Zheng N., Han Y., Xiao G., Ni M., Xu H., Dynamic simulation of a reversible solid oxide cell system for efficient H2 production and power generation. Energy 2023;263:125725.

[5] Chen H.Y., Jeng J.C., Integration of hydrogen production and greenhouse gas treatment by utilizing nitrogen oxide as sweep gas in a solid oxide electrolysis cell. Journal of the Taiwan Institute of Chemical Engineers 2022;130:103937.

[6] Wierzbicki M., Jagielski K., Niemczyk A., Chmielewski M., Impact of sweep gas on the degradation of an La0.6Sr0.4Co0.2Fe0.8O3-delta anode in a solid oxide electrolysis cell. Energies 2024;17(5):1144.

[7] Lim J., Lee W., Jeong K., Chu I., Hong J., Controlling the internal pressure drops of a kW-scale solid oxide electrolysis cell stack for the uniformity of flow distribution and reaction environment. Applied Energy 2025;383:125368.

[8] Lee W., Lang M., Costa R., Lee I.S., Lee Y.S., Hong J., Enhancing uniformity and performance in solid oxide fuel cells with double symmetry interconnect design. Applied Energy 2025;381:125178.